Engineering complex oxide interfaces for oxide electronics

Roy, Saurabh

Manuscripts: S. Roy *et al.*, **1.** *Probing hot electron transport across an epitaxial Schottky interface of $SrRuO_3$/Nb:$SrTiO_3$* Appl. Phys. Lett. **102**, 192909 (2013). **2.** *Engineering the interfacial energy profile across non-polar heterointerfaces*, submitted.

Chapter 5

Engineering interfacial energy profile across non-polar heterointerfaces

Abstract

Oxides heterointerfaces show a range of novel phenomena not present in their bulk form, thus providing an additional knob to tune the functional properties across such interfaces. Here we show that for an oxide Schottky interface between metallic $SrRuO_3$ and semiconducting Nb-doped $SrTiO_3$, the terminating surface of the substrate plays a crucial role in the electronic transport behaviour across it. This is manifested as the differences in the height of the Schottky barriers at the SrO and TiO_2 surface terminations of the substrate. The origin lies in the different interfacial atomic plane stacking of $SrRuO_3$, as confirmed by High-Resolution Scanning Transmission Electron Microscopy (HR-STEM) studies. First-principles density functional theory calculations conform with our experimental findings. The crucial role of the terminating atomic plane of the substrate in controlling Schottky barriers across non-polar oxide heterointerfaces is a new step towards the realization of novel functionalities in oxide based devices.

5.1 Introduction and Motivation

Complex oxide heterointerfaces are of immense interest in oxide electronics and have led to the emergence of new physical phenomenon that arises due to competing energy scales involved in the interplay between the structural, charge, spin and orbital degrees of freedom. Owing to the breaking of symmetry at these interfaces, novel interfacial physical properties like conduction [1], magnetism [2] and superconductivity [3] are exhibited, driving further research interest in these materials. Creating, engineering and characterizing such functional interfaces have been boosted by the evolution of sophisticated thin film techniques allowing the growth of atomically flat, lattice matched interfaces and probing them for their structure and electronic transport [4, 5, 6, 7, 8, 9, 10, 11]. As a result, many unique transport phenomena have been observed in devices with polar/(non)polar interfaces where the electronic properties are promoted by the presence of an electric field [14, 15, 16, 17, 18, 19]. In this context, although devices with non-polar oxide in-

terfaces have been studied [1, 12, 13], little focus has been given to the study of emerging functional properties at their heterointerfaces. The functional interface of metallic $SrRuO_3$ with an oxide semiconductor semiconductor Nb:$SrTiO_3$ Schottky interface provides an excellent template to study this.

The intriguing interface of $SrRuO_3$ and $SrTiO_3$ has attracted a lot of attention lately. Some recent studies demonstrated the evolution of magnetism with increasing thickness of $SrRuO_3$ and highlighted the crucial role the film/substrate interface plays in this regard [20, 21]. The same interface was studied for the influence of interfacial RuO_6 octahedral rotation on the magnetic anisotropy of the film, demonstrating the prominent role of the octahedral tilts on the physical properties [22]. Growth-wise, it has been reported that the surface terminating plane of the underlying substrate can significantly influence the initial growth of the deposited $SrRuO_3$ films and this has been proposed to be an interesting approach to fabricate ordered oxide nanostructures [23, 24]. As discussed in the previous chapter, the trenches that are created in thin films of $SrRuO_3$ are associated with a local surface termination of SrO on the $SrTiO_3$ substrate, where the initial growth of $SrRuO_3$ is unfavorable. Regions in between the trenches are areas of TiO_2 termination where $SrRuO_3$ film grows unhindered. Inspite of the recognized importance of the film/substrate interface, electronic transport across this interface has not been studied widely. This is in part due to the difficulties in obtaining non-invasive metrology methods to electrically probe the buried interface with a nanoscale resolution.

Here, we probe the metal-semiconductor interface of $SrRuO_3$ on Nb:$SrTiO_3$ and study the evolution of electronic transport for different thickness of the $SrRuO_3$ film (inside-outside the trenches). In this work, we use the technique of Ballistic Electron Emission Microscopy (BEEM) [28, 29] and use its local probing capabilities and high spatial resolution to investigate the differences in electron transport across $SrRuO_3$/Nb:$SrTiO_3$, at regions where the local termination varies between SrO and TiO_2. Using Scanning Tunneling Spectroscopy (STS), we find local variations of the surface conductivity as manifested by the differences in the local density of surface states in SRO at the trenches (region A) and outside them (region B). Based on the transmission of hot electrons perpendicular to the epitaxial Schottky interface of $SrRuO_3$/Nb:$SrTiO_3$, we observe variations in transmission using BEEM, between the two regions; the transmission is higher on the trenches (SrO termination) and corresponds to a larger Schottky Barrier Height (SBH). Such differences in the electronic landscape and its manifestation in different SBH could have multiple origin as the strain at the film/substrate interface or dislocations/defects created during growth. In order to establish the underlying correspondence between structure and

electronic transport, we engineer the interface between $SrRuO_3$ and Nb:$SrTiO_3$ by inserting a monolayer of SrO and find that such interface engineering leads to a clear difference in the potential landscape. A comparative study of the atomic structure at the film-substrate interface for both the devices was done using high resolution scanning transmission electron microscopy (HR-STEM). The high angle annular dark field (HAADF) intensity profiles clearly illustrate unequal displacements of the SrO and RuO_2 atomic planes of $SrRuO_3$ for both terminations. These observations are strongly correlated to the electronic properties of both interfaces, as observed from our transport studies. Such heterointerfaces of $SrRuO_3$ and $SrTiO_3$ were modeled to investigate the influence of substrate termination on the interfacial electronic properties.

5.2 Growth and fabrication of $SrRuO_3$ devices

Thin films of $SrRuO_3$ were grown by pulsed laser deposition (PLD) on Nb-doped (0.01 wt. %) $SrTiO_3$ (001) substrates while the surface quality was monitored by *in-situ* reflective high-energy electron diffraction (RHEED). It has been recognized that a clean and well defined substrate is imperative for the growth of uniform $SrRuO_3$ thin films and thus, we treat the substrates using the standard chemical protocol followed by an annealing at 960° C in oxygen, for 1.5 hrs to achieve a single TiO_2 termination of the Nb:$SrTiO_3$ substrates [25]. However, during the annealing process, Sr diffuses out to the steps resulting in occasional SrO terminations along with TiO_2 terminated regions on the substrates (described in chapter 4). Figure 5.1 shows the local SrO terminations of the chemically treated substrate, alongside the TiO_2 terminated regions. These have been circled as region A and region B, respectively. The height profile, from the AFM topography, corresponds to a step height of ~ 1 u.c. (0.4 nm) for region B and 0.2 nm for region A (the latter resembling a SrO terminated region).

Consequently, when a thin film of $SrRuO_3$ is grown on such double terminated substrate (T-Nb:STO), owing to dissimilar growth rates on SrO and TiO_2 terminations, long trenches are formed on the substrates. These reflect the growth preference of $SrRuO_3$ on the underlying termination of Nb:$SrTiO_3$; and is observed to be faster on TiO_2 terminated regions than on SrO terminations. Such disparate growth as seen in the atomic force microscopy (AFM) image in Figure 5.2 has also been marked as region A and region B corresponding to trenches along the film plane in SrO terminated regions and terraces (regions in between the trenches) correspond-

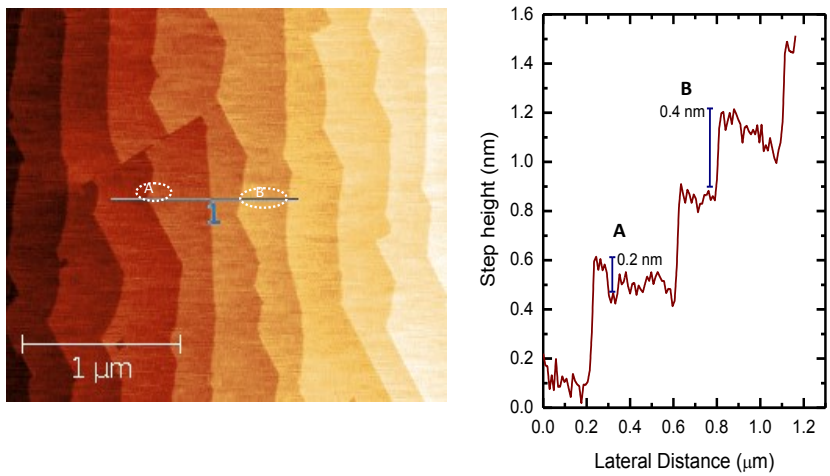

Figure 5.1: *AFM topography image of chemically treated Nb:$SrTiO_3$ substrate. In the corresponding step height profile, A corresponds to SrO terminated areas and B corresponds to TiO_2 terminations.*

ing to TiO_2 terminated regions, respectively. Although the growth of $SrRuO_3$ in SrO terminated regions of the substrate (region A) is non-uniform, typical depth of such trenches are close to 2.7 nm, indicating that the thick $SrRuO_3$ film on the TiO_2 terminated regions is $\sim$ 8 u.c. thick, and the thin $SrRuO_3$ film on the SrO terminated regions is $\sim$ 1.5 - 2.5 u.c. thick. Furthermore, the local SrO terminated regions of the substrate are usually confined small pockets ($\sim$ 40 nm in width) and growth of $SrRuO_3$ in similar locations could be accompanied by structural distortions, dislocations and defects which strongly influences the electronic properties of the deposited material. A recent study shows the impact of local strain on the physical phenomena on an otherwise highly epitaxial oxide thin film [34]. To discard such local influences, $SrRuO_3$ was deposited at MESA+, University of Twente with a monolayer of SrO on a TiO_2 terminated substrate (S-Nb:STO).

Although the chemical protocol to obtain TiO_2 termination is well established, no chemical treatments have been reported to produce the opposite single-terminated SrO surfaces. The single-terminated SrO surfaces can be obtained by deposition of a SrO monolayer on a single-terminated TiO_2 surface. For epitaxial SrO monolayer growth, pulsed laser interval deposition was applied [26]. In this deposition technique, the total number of laser pulses for one monolayer has to be provided rapidly (50 Hz) to stabilize the correct SrO layer without multilevel islands. Concerning the

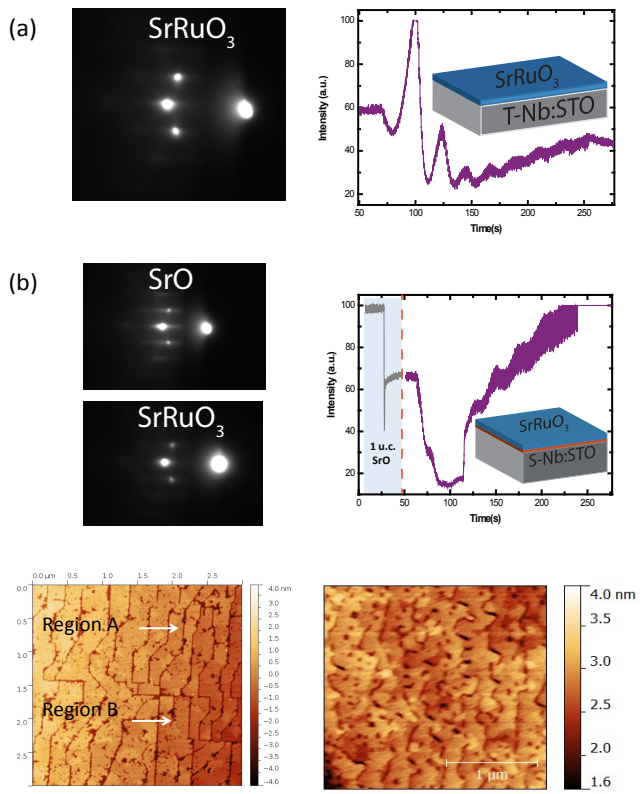

Figure 5.2: *Growth of 8 u.c. of $SrRuO_3$ on TiO_2 and SrO terminated substrates. (a) RHEED data for $SrRuO_3$ growth on non-engineered substrate T-Nb:STO. (b) RHEED data for the growth of a monolayer of SrO followed by 8 u.c. of $SrRuO_3$. (c) AFM scan image of T-Nb:STO and S-Nb:STO.*

deposition conditions, a single-crystal SrO target is ablated with an energy density of 1.3 J/cm^2. During growth, the substrate is held at 850° C (T_{dep}) in an oxygen environment at 0.13 mbar. This results in crystalline SrO-terminated $SrTiO_3$ surfaces with perfectly straight step edges [27]. Subsequently, $SrRuO_3$ thin films of 8 unit cells (u.c.) was deposited on SrO-Nb:$SrTiO_3$ substrates. Figures 5.2(a,b) show the RHEED specular spot intensity during the deposition of $SrRuO_3$ on T-Nb:STO and for the growth of one monolayer of SrO followed by 8 u.c. of $SrRuO_3$ respectively. The oscillations of the RHEED intensity indicates a partially layer-by-layer growth mode in both cases. The corresponding RHEED diffraction images clearly show

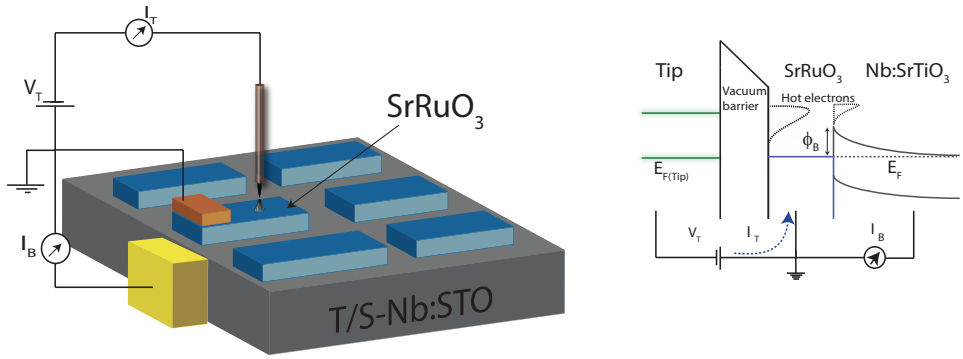

Figure 5.3: *(a) Fabrication of multiple $SrRuO_3$ devices of grown on Nb:$SrTiO_3$. Analyses were done on many different devices to understand the electronic behavior of the film-substrate interface. (b) Schematic diagram of BEEM, where the Pt-Ir STM tip injects hot electrons over the vacuum barrier into a thin metallic film of $SrRuO_3$. The transmitted electrons that satisfy the energy and momentum criteria to overcome the SBH at the interface are collected in the Nb:$SrTiO_3$ semiconductor.*

sharp two dimensional spots, indicating diffraction from smooth crystalline surfaces. Figure 5.2(c) show the AFM images of the 8 u.c. $SrRuO_3$ grown on both types of single-terminated surfaces. The low level of surface roughness was confirmed for both cases as the micrographs and roughness analyses show smooth terraces with unit cell steps.

The as-grown films were then patterned into devices using UV lithography and Ion Beam etching (IBE). Figure 5.3 shows the measurement scheme including the design of the sample being measured. An Ohmic back contact was realized by evaporating Ti/Au over a large area, which acts as the collector in this transport geometry. The devices were transferred into an ultra-high vacuum (UHV) scanning tunneling microscopy (STM)/BEEM system for measurement. The measurements were conducted at room temperature (300 K). The three terminally modified version of STM is used to study carrier transport through the buried M-S interface, at different energies, with high spatial resolution [28, 29, 30, 31]. The tip of an STM is used as an emitter and is set to a bias -V_T resulting in the injection of a distribution of hot electrons into the $SrRuO_3$ metal base. Upon injection, they undergo scattering and a few hot electrons, after transmission through the $SrRuO_3$ film are collected in the conduction band (CB) of Nb:$SrTiO_3$. The Schottky barrier (ϕ) at the M-S interface acts as an energy filter, allowing only those electrons to pass through

that have enough energy to overcome the barrier. In other words, while doing spectroscopy studies no BEEM current (I_B) is observed for a voltage below a threshold value when the electrons do not possess enough energy to overcome the ϕ at the M-S interface. The energy schematics of BEEM is shown in Figure 5.3. In our studies, the BEEM current (I_B) is recorded at different local regions of the device. The BEEM transmission depends exponentially on the thickness of the $SrRuO_3$ (d_{SrRuO_3}) film and can be expressed as [32, 10] :

$$\frac{I_B}{I_T} \propto exp[-\frac{d_{SrRuO_3}}{\lambda_{SrRuO_3}(E)}] \tag{5.1}$$

where λ_{SrRuO_3} is the hot electron attenuation length and I_T is the tunnel current. In accordance to the Bell-Kaiser model (B-K), the local SBH at the $SrRuO_3$/Nb:$SrTiO_3$ interface is given by:

$$\sqrt{\frac{I_B}{I_T}} \propto (|V_T| - \phi_B) \tag{5.2}$$

5.3 Results and discussions

The devices were first investigated for their electrical transport across the Schottky interface. Figure 5.4(a) shows the room temperature (RT) I-V characteristics of a 8 u.c. $SrRuO_3$ film on Nb:$SrTiO_3$. The rectification is as expected for a Schottky diode between a metal and an n-type semiconductor. The linear increase in current with bias as seen in the forward characteristics of the diode can be fitted with the thermionic emission model given by:

$$I = AA^*T^2 exp(-\frac{q\phi}{k_BT}) \left[exp(\frac{qV}{nk_BT}) - 1\right] \tag{5.3}$$

The symbols have their usual meanings [33]. From the linear part of the forward characteristics of the diode, the SBH, ϕ, was determined to be 1.15$\pm$0.02 eV with an ideality factor n = 1.1. This indicates thermionic emission to be the dominant transport mechanism across the Schottky interface.

For the BEEM studies, a large area contact to the rear of the semiconducting substrate was used to collect the hot electrons after transmission through the $SrRuO_3$ film and across the Schottky interface. All the measurements were performed at RT (300 K). The STM surface topography of the T-Nb:STO device, recorded at -1 V and 1 nA, is shown in Figure 5.4(b). It is observed that the surface topography replicates the AFM image, and here too trenches and terraces are clearly visible as shown in A and B respectively. Average width of these trenches running along the sample is

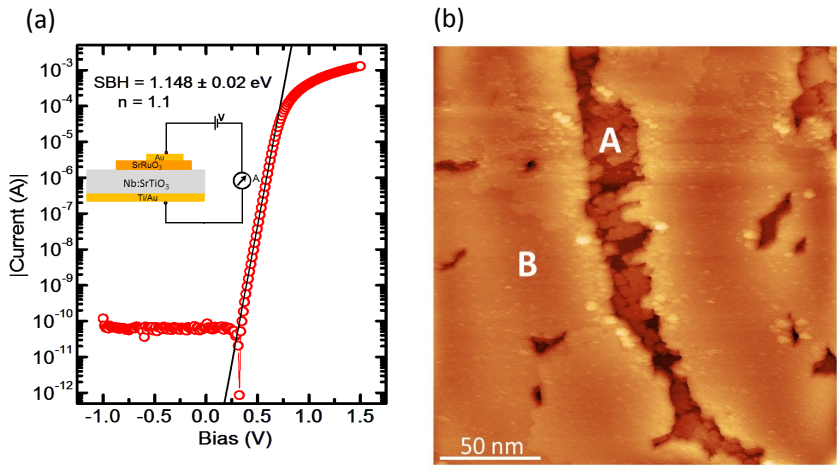

Figure 5.4: *(a) Current (I)-voltage (V) characteristics of the $SrRuO_3$/Nb:$SrTiO_3$ Schottky diode. The straight lines indicate the thermionic emission theory fitted to obtain the Schottky barrier height and ideality factor of the diode. (b) A STM topography scan of an 8 u.c. thick $SrRuO_3$ film on Nb:$SrTiO_3$ at V_T=-1 V and I_T=-1 nA. Thermal annealing of the substrate leads to out diffusion of Sr to the surface and finally to step edges. The slower growth of the initial $SrRuO_3$ layer at the SrO terminated areas results in the formation of trenches as shown in region A. Region B is the area in between the trenches.*

around 30-40 nm. As the technique of BEEM is spatially resolved, we can record a large number of BEEM spectra both inside and outside the trenches. BEEM transmission was recorded for many such trenches across several devices. The representative average BEEM spectra across SrO termination in T-Nb:STO is shown in Figure 5.5. Figures 5.5(b) and 5.5(c) correspond to region A and region B, respectively. In both cases, we observe a sharp onset in I_B beyond a certain tip bias voltage which corresponds to the local Schottky Barrier Height at the metal-semiconductor interface. It is observed that transmission in region A is an order of magnitude higher than region B. This can be understood by the fact that I_B exponentially decreases with increasing thickness of the metal layer, [29, 28] which in region A is thinner than in region B. The local SBH at the different regions can be extracted from their respective I_B plots using an approximation of the B-K model (under standard assumptions of planar tunneling, and free electron dispersion relation in STM tip and base metal) by plotting the square root of the BEEM current (I_B) versus tip bias (V_T),

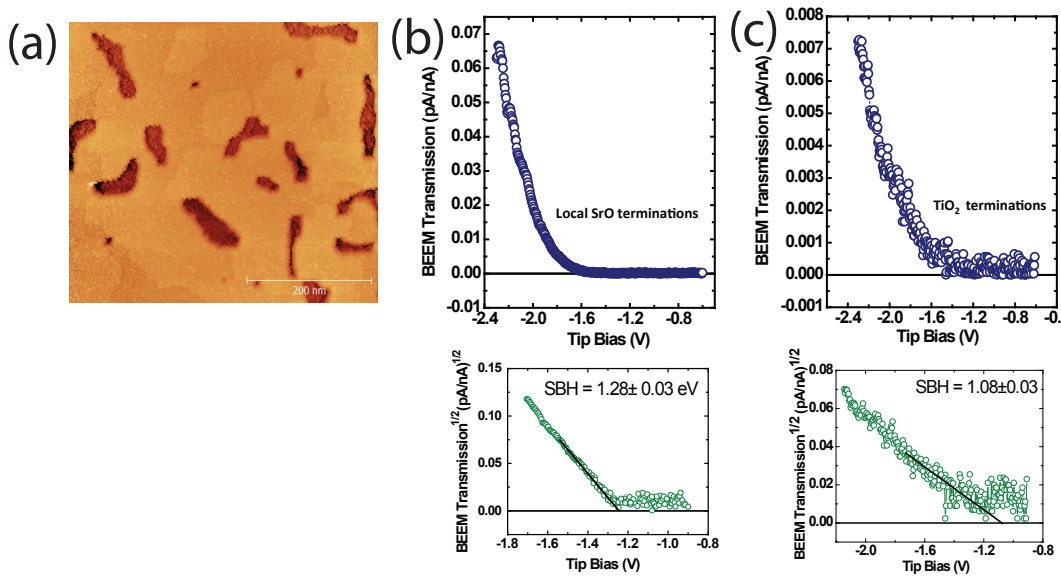

Figure 5.5: *(a) STM topography of 8 u.c. of $SrRuO_3$ grown on T-Nb:STO at V_T = -1.4 V and I_T = 4 nA. Occasional dark patches indicate thinner $SrRuO_3$ grown on SrO terminations of the substrate. (b) Corresponding BEEM spectra for tip placed in dark patches (trenches) i.e. on SrO terminations of the substrate. The extracted corresponding local SBH is represented below. (c) BEEM spectra for tip placed on TiO_2 terminated regions, i.e. on thicker $SrRuO_3$ growth. Corresponding local Schottky barrier height below.*

as per Eqn. 5.2.

The intersect of the straight line with the voltage axis gives the local SBH, which for region A is found to be 1.27±0.03 eV and 1.11±0.03 eV for region B as shown in Figures 5.5(b) and 5.5(c), respectively. Thus, we find local differences in the energy band alignments at the M-S interface in regions A and B. We recall that from standard current-voltage studies, a unique value for the SBH corresponding to 1.15±0.02 eV was obtained (Figure 5.4(a)), which matches closely to that obtained from region B using BEEM. For the extraction of the SBH, the experimental data were fit close to the threshold (up to 200 meV above the threshold), and the error bar was determined by considering the spread of the BEEM transmission near threshold.

As the local SrO terminated regions in T-Nb:STO are mostly confined to the terrace edges and occur in small pockets, it is not apparently clear whether the growth

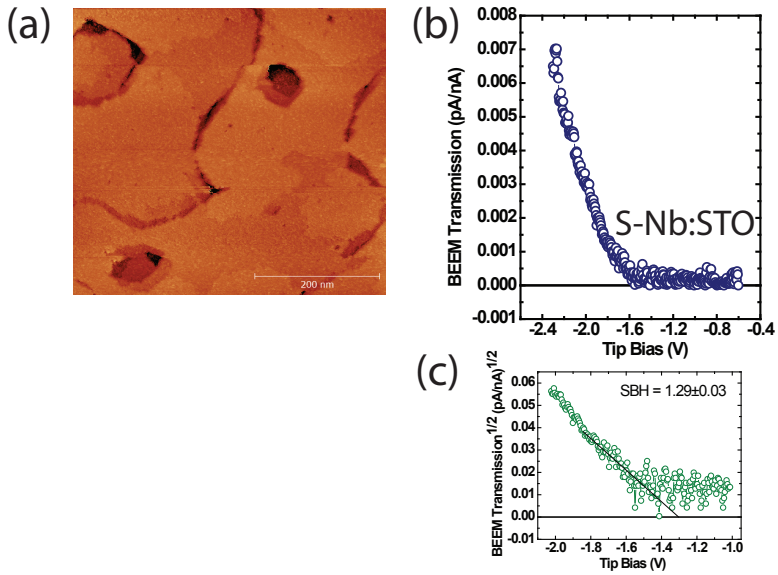

Figure 5.6: *(a) STM topography of 8 u.c. of $SrRuO_3$ grown on S-Nb:STO at V_T=-1.4 V and I_T=4 nA. (b) Corresponding BEEM spectra through 8 u.c. of $SrRuO_3$ grown on S-Nb:STO. (c) The extracted local Schottky barrier height. Clearly, the local SBH matches with that extracted from $SrRuO_3$ grown inside the trenches of T-Nb:STO.*

of $SrRuO_3$ in such confined regions could alter the electronic property at the interface by possible occurrences of defects and changes in local strain. In order to rule out any such contributions to the band alignment at the interface, we engineer the substrate terminating layer as is done in S-Nb:STO. We study electronic transport across it using BEEM and compare the extracted local SBH with that obtained for $SrRuO_3$ grown inside the trenches of T-Nb:STO. Figure 5.6(a) shows the STM topography image of the top surface of $SrRuO_3$ grown on S-Nb:STO. By locating the tip on the flat regions of the terraces, several BEEM spectra were obtained and an average of such spectra taken on several such regions is shown in Figure 5.6(b). By fitting the B-K model, we extract the local SBH (Figure 5.6(c)). Our findings highlight two key features:

- A comparison of the BEEM transmission at SrO terminations in Figures 5.5 (b) and 5.6 (b) shows that it is higher in T-Nb:STO than in S-Nb:STO. This deviation, of an order of magnitude, is a result of the variation in thickness of $SrRuO_3$ on SrO terminations on either substrates. The growth rate in local SrO terminated pockets is lower than on the terraces of T-Nb:STO, and thus the

thickness of $SrRuO_3$ grown inside the trenches are less than 8 u.c. However for S-Nb:STO, an uniform 8 u.c. of $SrRuO_3$ is grown on the engineered interface which is thicker than the above and thus results in a lower BEEM transmission in this case.

- The local SBHs extracted from the different SrO terminations for both devices (T-Nb:STO and S-Nb:STO) yield the same value of 1.28$\pm$0.03 eV.

It is fascinating to find that such a deliberate design of the oxide interface by merely changing the surface termination at the interface can influence the electronic transport across such non-polar interfaces. Further, this measurement confirms that the different energy band line-ups at the M-S interface is truly governed by the terminating layer of the substrate, and is thus an intrinsic property of the interface itself.

In addition to capturing topography images and locally probing the buried M-S interface, scanning tunneling spectroscopy (STS) studies were also done at these local regions (SrO and TiO_2 terminations in T-Nb:STO) to gain insights into the local electronic structure of the surface of $SrRuO_3$. When performing STS measurements, the tip is held at a fixed position above the sample to eliminate the effect of topography changes on the tunneling current. Tunneling conductance spectra were recorded by varying V_T. The feedback loop of the STM was disengaged and the bias voltage was swept through the desired voltage range to record each spectrum. Upto 200 spectra were recorded each for regions A and B as shown in Figure 5.7(a,b). From the STS spectra, the terraces are found to be more metallic than the trenches and ascribed to the increased thickness of the $SrRuO_3$ at these locations, owing to the favorable underlying TiO_2 terminations in the substrate. From earlier reports, it is well known that the metallicity and conductance of $SrRuO_3$ films increases with increasing thickness and our findings are in line with the previous studies.[35]

A careful study of the interfaces for T-Nb:STO and S-Nb:STO reveals that the interface termination sequence is always $TiO_2/SrO/RuO_2$, regardless of the initial substrate termination. Irrespective of this, the electrostatic potential at the M-S interface is different for T-Nb:STO and S-Nb:STO which raises concerns about its origin. Spatially resolved HAADF-STEM imaging was performed to further investigate the exact atomic arrangement at the film/substrate interface for both the T-Nb:STO and S-Nb:STO devices. The transmission electron microscopy studies were done at University of Antwerp. Figures 5.8(a) and 5.8(c) show the high resolution HAADF images of the films, demonstrating the high quality and epitaxial growth of the film in both devices. The brighter region corresponds to the $SrRuO_3$ films and the darker region to the Nb:$SrTiO_3$ substrate.

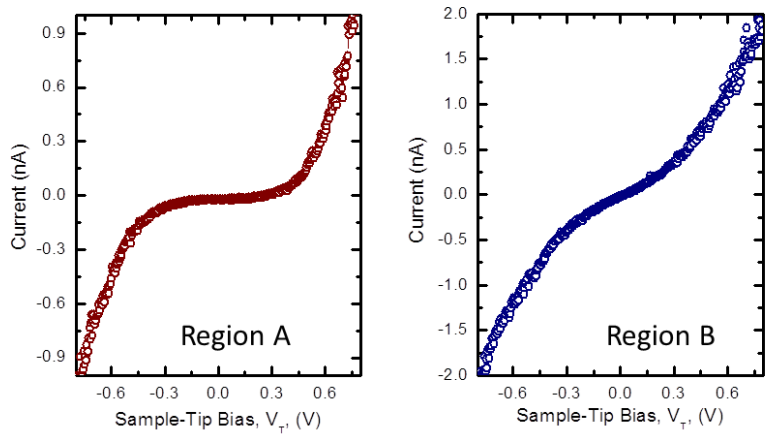

Figure 5.7: *Scanning tunneling spectroscopy spectra acquired at regions A and B at RT by sweeping the applied bias as shown. Region B is found to be more metallic than region A.*

As HAADF-STEM is sensitive to the projected average atomic number within an atomic column, it can be used to position the location of the cations across the film/substrate interface. Figures 5.8(b) and 5.8(d) show the HAADF intensity line profiles crossing the Ti, Ru (white lines) or half a unit cell shifted crossing the Sr atoms (grey lines). In T-Nb:STO, the stacking of the $(SrRuO_3)_6$-RuO_2-SrO-**Ti**O_2-SrO-TiO_2-$(SrTiO_3)_n$ atomic planes are estimated as expected by nominal growth conditions. Note that: (i) the 8^{th} unit cell of $SrRuO_3$ might be hidden by the deposition of the protection layer and (ii) the slightly higher peak intensity at the interfacial TiO_2 layer when compared to the ones further below in the Nb:$SrTiO_3$ substrate can be attributed to the small amount of Ru inter-diffusion upto 1 monolayer into the substrate or some tail effects due to the neighboring Sr columns. In the case of S-Nb:STO, the presence of both SrO and TiO_2 interfacial layers are observed as a result of the substrate atomic step indicated by arrows in Figure 5.8(b). Here the stacking of the $(SrRuO_3)_7$-SrO-RuO_2-**SrO**-TiO_2-$(SrTiO_3)_n$ atomic planes can be clearly identified.

The structural distortions are estimated across the film/substrate interface leading to some interesting observations. For S-Nb:STO, the lattice distortions measured

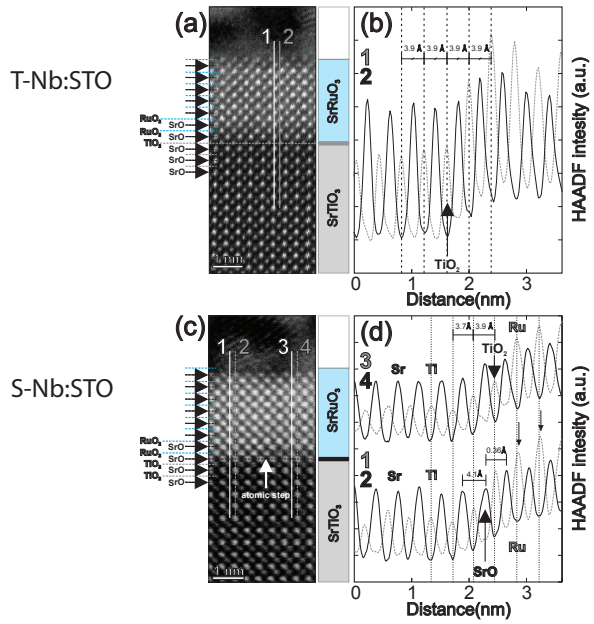

Figure 5.8: *(a) HAADF-STEM image of 8 u.c. of $SrRuO_3$ on T-Nb:STO. Red and green line sections are guide to realize the cationic positions of Ru/Ti and Sr across the film/substrate interface. (b) The intensity profiles of the cationic positions are mapped across either sides of the interface. (c) HAADF-STEM image of 8 u.c. of $SrRuO_3$ on S-Nb:STO. An atomic step is observed in the section view. Line sections are drawn on either sides of the atomic step to realize cationic positions. (d) Intensity profiles are plotted to understand the displacement of atomic planes across the interface.*

along the film growth direction (c-axis) causes either an increased (c=4.1 Å) or reduced (c=3.6 Å) unit cell parameter at the film/substrate interface whereas no variation from the nominal c=3.9 Å is observed for T-Nb:STO. Note that the Ti and Ru atomic positions on the left side of the atomic step slightly deviate from the ones obtained on the right side, as indicated by small vertical arrows in Figure 5.8 (d). These structural distortions can originate as a result of compressive strain at the interface between the cubic $SrTiO_3$ substrate (a=3.905 Å) and the orthorhombic $SrRuO_3$ (pseudo-cubic lattice parameter a_p=3.93 Å), which further relaxes already after 1 u.c. Such an abrupt increase of the interlayer distance at the interfaces is suggested to give rise to a definite polar character to the interface. Unfortunately, our samples reported sever degradation to the electron beams for electron energy loss spectroscopy (EELS) measurements that prevented a direct determination of

the electronic structure of the interfaces.

Consequently, the technique of low-loss EELS was carefully employed to probe the electronic structure of the M-S interface. Low-loss EELS is traditionally described by energy loss processes observed between 0-50 eV region of the spectrum. The interactions of electrons with the specimen result in electrons being excited into unoccupied energy levels within the conduction band, as well as collective excitation of valence electrons. These collective excitations provide key insights into the electronic properties. When such an electron beam is focused at the interface, the obtained spectrum could be analyzed for energy losses pertaining to various electronic transitions, locally around the M-S interface. These energy loss spectra contain important information for several interband transitions, with a possibility to indicate the transition across a Schottky barrier. As such an interband transitions are caused by electrons being excited within the valence band and then entering the empty states of conduction bands, both the S-Nb:STO and T-Nb:STO samples were probed for their low-loss EELS spectrum.

Figure 5.9 (a) shows the low-loss EELS spectra for $SrRuO_3$/T-Nb:STO (green) and $SrRuO_3$/S-Nb:STO (black) thin films. For both the samples, the zero loss peak (ZLP), which mainly contains electrons that still possess the original beam energy have been removed. We observe that either spectra (for both the samples) show two intensity peaks; the sharper peaks occur at 1.08 eV and 0.9 eV for T-Nb:STO and S-Nb:STO, respectively. They further possess spectral features at 2.0 eV (S-Nb:STO) and 2.2 eV (T-Nb:STO), although the intensity peak profile is fatter than the previous ones. As mentioned, such peaks are indicative of transitions in the band structure model but to indicate precisely the transitions, it is critical to point out the electronic states around the M-S interface. Figure 5.9 (b) illustrate the possible electronic transitions at the interface responsible for the intensity peaks in the low-loss EELS spectra around the M-S interface.

Accordingly, an increased intensity profile representative of the transition from the occupied state of $SrRuO_3$ across the Schottky barrier height should be expected to appear at 1.11 eV and 1.28 eV for T-Nb:STO and S-Nb:STO, respectively which is absent in the low-loss EELS data. Instead, the spectral features at 1.08 eV and 0.9 eV are possible indications of transitions to in-gap states as the intensity drops thereafter. Although at higher energies the spectral shape regains the intensity, such transitions can not be ascribed to the SBH for the samples. Thus, our data (Figure 5.9 (a)) does not show a clear signature of transitions corresponding to the SBH. Again, as no earlier studies have been performed in this direction, a closer look needs to

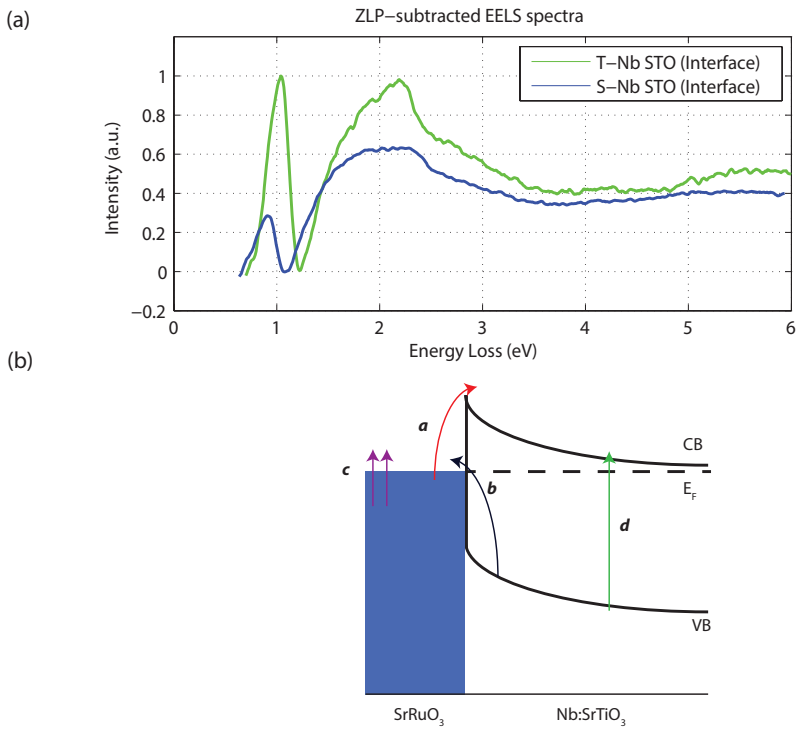

Figure 5.9: *(a) Background-subtracted low-loss EELS spectra for the $SrRuO_3$/T-Nb:STO (green) and $SrRuO_3$/T-Nb:STO (black) thin films. (b) A simplified model of the band alignment diagram in the $SrRuO_3$/Nb:$SrTiO_3$ thin films. Transition a represents the electronic transition from the Fermi level of $SrRuO_3$ to the unoccupied energy level in the conduction band of Nb:$SrTiO_3$. Such a spectral shape would indicate a transition across the Schottky barrier, thus providing the measure of the energy scale at which the transition takes place. b represents the transition from the top of the valence band in the semiconductor to the unoccupied energy level in $SrRuO_3$. (c) indicates the energetic transitions from the Fermi level of $SrRuO_3$ to the higher unoccupied states, and d is a representation of transition across the band gap of the semiconductor.*

be taken at the to identify any coherency between the energy loss signal and the interpretation of the barrier height. In further experiments which are planned for the samples, investigation of the ZLP might provide vital information from the EELS spectra.

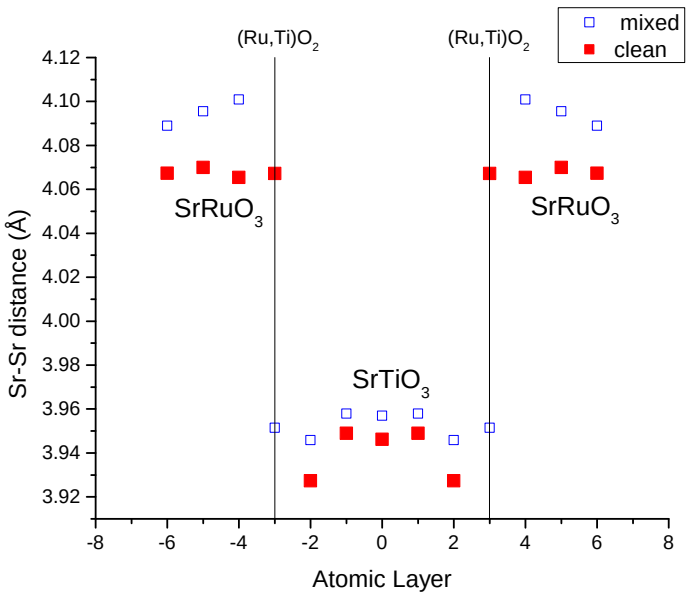

Figure 5.10: *(a) Layer-by-layer metal-oxygen displacements of the $SrRuO_3/SrTiO_3$ supercell used to simulate the T-Nb:STO interface. Solid symbols indicate the (Ru,Ti)O2 atomic layers, and open symbols correspond to the SrO atomic layers. (b) Same as in (a) but for the S-Nb:STO interface.*

Unlike polar heterointerfaces, the difference of electronic structure in T-Nb:STO and S-Nb:STO devices should have an intrinsic origin at the interface. Although the two M-S interfaces are ideally non-polar; it requires an induced dipole at the interface to bring about the change in the SBH. However, the occurrence of such an induced dipole is puzzling at the symmetric $SrRuO_3/Nb:SrTiO_3$ interface. One possible reason for a dilatation of the c-axis parameter for the first monolayer of $SrRuO_3$ on S-Nb:STO could be a small amount of intermixing of the Ru/Ti sites. Owing to the different surface energies of the SrO and TiO_2 terminations of $Nb:SrTiO_3$ substrates, a more thermodynamically stable interface could result by exchanging cations between Ru and Ti sites for S-Nb:STO, rather than an abrupt interface [36]. From our cross-section overview for T-Nb:STO and S-Nb:STO, no apparent intermixing could be observed but such an occurrence can't be ruled out owing to the close match of the ionic radii of Ru^{4+} and Ti^{4+} (Ru^{4+} = 76 pm and Ti^{4+} = 74 pm). SrO and TiO_2 have different surface energies and this difference could drive an in-

termixing of the Ru and Ti ions on S-Nb:STO which lowers the surface energy of the interface. Considering such a scenario, a first principles DFT calculation was performed where the M-S interface for S-Nb:STO was simulated with a 50% intermixing of Ru and Ti ions and a pristine interface for T-Nb:STO. The supercells are constructed by stacking these structural unit cells of $SrRuO_3$ and $SrTiO_3$ along the [001] direction (z direction). We consider two cases for the interface terminations as shown in Figure 5.10. First we study a supercell with TiO_2 terminated substrate (T-Nb:STO) on both interfaces and, second, another supercell with SrO termination (S-Nb:STO). Both supercells are fully atomically relaxed until forces are less than 20 meV/Å with the constraint that the in-plane lattice constant of the supercell to be calculated has lattice constant of cubic $SrTiO_3$, a=3.9 Å to simulate epitaxial growth on an $SrTiO_3$ substrate. Results of the relaxation for both cases are shown in Figure 5.10. For the interface at T-Nb:STO, only a small out-of-plane metal/oxygen displacement is present, indicating that the structure is close to the natural continuation of both perovskite structures at the interface, as concluded experimentally. For the S-Nb:STO interface, however, large displacement of the Sr sites with respect to oxygen sites is apparent as discussed previously. The large difference in displacement profile between the two types of interface terminations are expected to lead to a significant difference in the electrostatic interface dipole between $SrRuO_3$ and $SrTiO_3$, and should therefore be apparent in the electronic band line-up. Indeed, this is the case as can be seen in the local density of states (LDOS) deep inside the $SrTiO_3$ as shown in Figure 5.11. It is observed that the variation of the interface composition leads to a linear change of the $SrTiO_3$ conduction band offset with respect to the T-Nb:STO and hence to a linear change of the Schottky barrier height at this interface. Indeed we see that the S-Nb:STO interface has an n-type SBH 0.19 eV larger than the T-Nb:STO interface. This is remarkably similar to the experimentally measured difference in n-SBH between the S-Nb:STO and T-Nb:STO. Furthermore, the enhanced displacements observed in the HR-STEM for the S-Nb:STO interface are consistent with the large displacements found in our DFT calculations.

Having quantitatively demonstrated the evolution of band alignment at the M-S interface with intermixing, we present another reason for the enhanced atomic plane distance at S-Nb:STO. A different amount of oxygen vacancies at the interfaces of S-Nb:STO and T-Nb:STO, as a recent report suggests, could thus play an important role in the structural distortion for S-Nb:STO [37]. The presence of oxygen vacancy in the SrO plane significantly reduces the electron repulsion in that direction (c-axis) and that results in an increased displacement between the atomic planes at the interface. This also impacts Ti-O-Ru bond angle at the interface which alters the local electrostatic potential at the $SrRuO_3$/S:Nb:STO interface. These oxygen vacancies

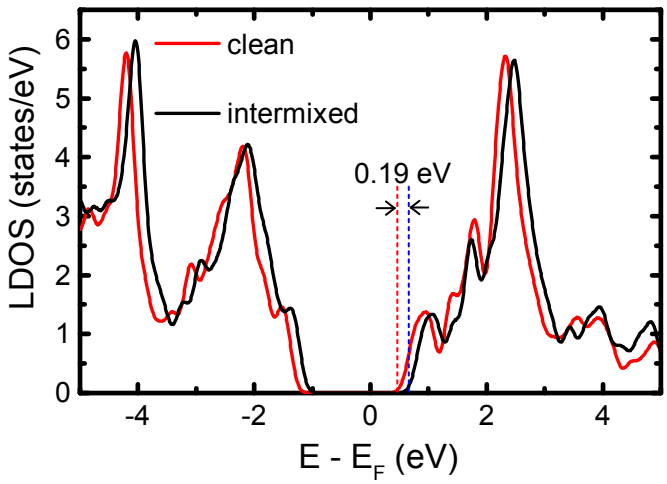

Figure 5.11: *The local density of states (LDOS) in the center of the $SrTiO_3$ for both interface terminations. Vertical dashed lines indicate the position of the conduction band minimum (CBM) with respect to the Fermi level, E_F.*

reduce the coordination of the Ru ion and affects the Ru d-orbital splitting in S-Nb:STO. For T-Nb:STO (with no oxygen defects), the d_{xy}, d_{xz} and d_{yz} orbitals are lower in energy than the d_{z^2} and $d_{x^2-y^2}$. On the other hand, for the distorted structure with oxygen vacancies, there is a further splitting in the Ru d orbitals where d_{xz} and d_{yz} are lower in energy than d_{xy}, and d_{z^2} further lowered in energy with respect to $d_{x^2-y^2}$ due to the decreased electron repulsion along the c-axis [38]. With no oxygen vacancies for the T-Nb:STO, the energy band line-up at the interface is thus different from that of S-Nb:STO, thereby supporting the different SBH.

While it may be certainly reasonable to consider the different number of oxygen vacancies to be creating the different electronic structure at the two interfaces (S-Nb:STO and T-Nb:STO), we present a third reason for the observation of different SBH. This arises from the different electronic structures of $SrTiO_3$ for SrO and TiO_2 terminations. At the surface layer, all the cations are pushed into the substrate as compared with an ideal surface, the Ti and Sr move deeper than the oxygen atoms, leading to a surface buckling. For the SrO interface, the Sr atom moves inwards more in S-Nb:STO as compared to the Ti atoms of T-Nb:STO. A key aspect of this effect is a net surface induced electric polarization which arises due to the oxygen-cation relative displacements along the c-axis. The crucial difference among the two

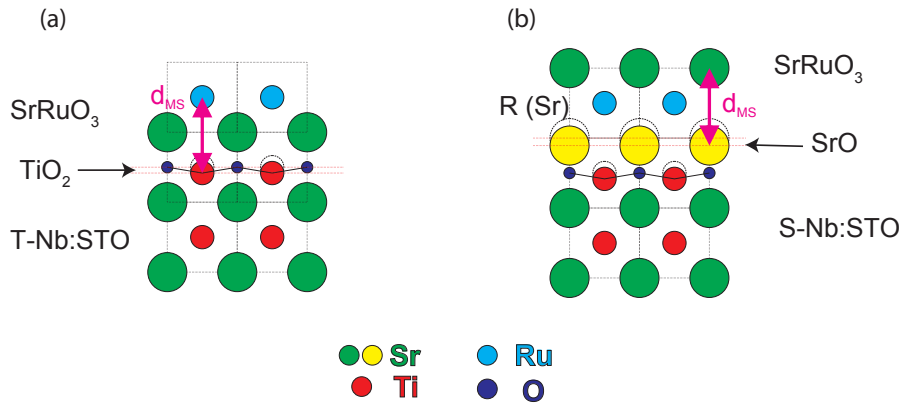

Figure 5.12: *A representative ball and stick model of the interface reconstruction for S-Nb:STO and T-Nb:STO. Owing to different surface rumpling for the two interfaces, the $SrRuO_3$ film grown on top develops different distance of separation between the cations (d_{MS}). This results in unequal dipole contributions thereby causing different potentials, manifesting as the differences in SBH at these interfaces.*

terminations is the magnitude of this dipole moment which changes the local electrostatic potentials of SrO and TiO_2 terminations of Nb:$SrTiO_3$ [39]. Subsequently, when $SrRuO_3$ is grown on either terminations under same growth conditions, it may be difficult to release this local electrostatic disturbance which is trapped at the interface, thereby manifesting as different energy band alignments for S-Nb:STO and T-Nb:STO. This is illustrated in Figure 5.12.

To figuratively understand the difference in the band line-ups, we make an analogy with the bond polarization theory proposed Tung [40] by invoking the interaction between the chemical bonds with the different dipoles at the local M/S interfaces. In this model, the SBH is written as

$$\phi = \gamma_B(\phi_M - \chi) + (1 - \gamma_B)\frac{E_g}{2} \tag{5.4}$$

where γ_B is the strength of the interface dipole and expressed as

$$\gamma_B = 1 - \frac{q^2 N_B d_{MS}}{\epsilon_{it}(E_g + \kappa)} \tag{5.5}$$

N_B is the number of bonds at the M/S interface, E_g is the band gap of the semiconductor, ϵ_{it} is the dielectric screening at the interface, d_M is the distance between

the metal and semiconductor atoms at the interface and κ is the sum of all the hopping interactions between neighboring atoms at the interface. Such a model, that takes into account the dipole density at the M/S interface, has been used by Hikita et al. [43], along with polarity mismatch at the Schottky interface to explain the systematic increase in the SBH with increasing SrO coverage.

We know that in $SrRuO_3$, the Ru 4d states are split by an octahedral crystal field into t_{2g} and e_g bands and the latter are relevant for hot electron transport in SRO.[41] The $4d_{3z^2-r^2}$ orbitals in the e_g bands have a different spatial distribution as compared to the $d_{x^2-y^2}$ orbitals;[42] with the orientation of the former being along the interface and the latter parallel to the interface. This difference in spatial distribution and the distance of separation of the cations at the heterointerface will influence their interaction with the interface dipoles at the local SrO and TiO_2 terminated regions in Nb:STO, with the dipole strength decreasing at the SrO terminations and giving rise to a higher SBH (as also expected from Eqn. 5.4 and 5.5). At the TiO_2 terminated regions, the strong interaction with the $4d_{3z^2-r^2}$ orbitals oriented along the interface will increase the interface dipole strength and decrease the SBH. The strong influence of the underlying substrate termination to the growth of SRO thus gets manifested as local changes in the transport characteristics and their corresponding energy band lineups at the M/S interface which has been probed using the local probing capabilities in BEEM.

5.4 Conclusion

The high selectivity of SRO growth with regard to the different surface terminations at local regions of the substrate leads to local variations in the thickness of SRO which is studied using STM and STS. The main result of this research is the effect of engineering the termination of the substrate on electronic transport at the film/substrate interface. We investigate this using a vertical device scheme of $SrRuO_3$ on Nb:$SrTiO_3$ and engineer the Nb:$SrTiO_3$ interface by inserting a monolayer of SrO. Local differences in the SBH at the interface between engineered/non-engineered is 0.19 eV, thereby indicating different energy band line-ups. At the engineered interface, the differences in the spacing between the atomic planes leads to the occurrence of a polar character as compared to the non-engineered non-polar interface. Three such possible scenarios are discussed which could entail the root cause for such an observation. In each of them, a resulting surface morphology change would finally lead to a change in local dipole character of the interfaces, thereby manifesting as

differences in the SBH. This study emphasizes the extra control the substrate termination provides to the other degrees of freedom in complex oxides relevant for numerous applications.

Bibliography

[1] A. Ohtomo, H. Y. Hwang, *Nature* **2004**, 427, 423.

[2] A. Brinkman, M. Huijben, M. van Zalk, J. Huijben, U. Zeitler, J. C. Maan, W. G. van der Wiel, G. Rijnders, D. H. A. Blank, H. Hilgenkamp, *Nat. Mater.* **2007**, 6, 493.

[3] S. Thiel, G. Hammerl, A. Schmehl, C. W. Schneider, J. Mannhart, *Science* **2006**, 313, 1942.

[4] D. H. Lowndes , D. B. Geohegan, A. A. Puretzky, D. P. Norton, C. M. Rouleau, *Science* **1996**, 273, 898.

[5] H. N. Lee, H. M. Christen, M. F. Chisholm, C. M. Rouleau, D. H. Lowndes, *Nature* **2005**, 433, 395.

[6] D. G. Schlom, J. H. Haeni, J. Lettieri, C. D. Theis, W. Tian, J. C. Jiang, X. Q. Pan, *Mater. Sci. Eng. B* **2001**, 87, 282.

[7] M. P. Warusawithana, E. V. Colla, J. N. Eckstein, M. B. Weissman, *Phys. Rev. Lett.* **2003**, 90, 036802.

[8] M. Varela, S. D. Findlay, A. R. Lupini, H. M. Christen, A. Y. Borisevich, N. Dellby, O. L. Krivanek, P. D. Nellist, M. P. Oxley, L. J. Allen, S. J. Pennycook, *Phys. Rev. Lett.* **2004**, 92, 095502.

[9] M. Minohara, R. Yasuhara, H. Kumigashira, M. Oshima, *Phys. Rev. B* **2010**, 81, 235322.

[10] K. G. Rana, T. Yajima, S. Parui, A. F. Kemper, T. P. Devereaux, Y. Hikita, H. Y. Hwang, T. Banerjee, *Sci. Rep.* **2013**, 3, 1274.

[11] K. G. Rana, S. Parui, T. Banerjee, *Phys. Rev. B* **2013**, 87, 085116.

[12] A. Ohtomo, D. A. Muller, J. L. Grazul, H. Y. Hwang, *Nature* **2002**, 419, 387.

[13] S. Okamoto, A. J. Millis, *Nature* **2004**, 428, 630.

[14] N. Nakagawa, H. Y. Hwang, D. A. Muller, *Nat. Mater.* **2004**, 5, 204.

[15] N. Reyren, S. Thiel, A. D. Caviglia, L. Fitting Kourkoutis, G. Hammerl, C. Richter, C. W. Schneider, T. Kopp, A. S. Retschi, D. Jaccard, M. Gabay, D. A. Muller, J.-M. Triscone, J. Mannhart, *Science* **2007**, 317, 1196.

[16] A. D. Caviglia, S. Gariglio, N. Reyren, D. Jaccard, T. Schneider, M. Gabay, S. Thiel, G. Hammerl, J. Mannhart, J.-M. Triscone, *Nature* **2008**, 456, 624.

[17] Guneeta Singh-Bhalla, C. Bell, J. Ravichandran, W. Siemons, Y. Hikita, S. Salahuddin, A. F. Hebard, H. Y. Hwang, R. Ramesh, *Nat. Phys.* **2011**, 7, 80.

[18] Y. Hotta, T. Susaki, H. Y. Hwang, *Phys. Rev. Lett.* **2007**, 99, 236805.

[19] P. R. Willmott, S. A. Pauli, R. Herger, C. M. Schleptz, D. Martoccia, B. D. Patterson, B. Delley, R. Clarke, D. Kumah, C. Cionca, Y. Yacoby, *Phys. Rev. Lett.* **2007**, 99, 155502.

[20] F. Bern, M. Ziese, A. Setzer, E. Pippel, D. Hesse, I. Vrejoiu, *J. Phys. :Cond. Mat.* **2013**, 25, 496003.

[21] J. Xia, W. Siemons, G. Koster, M. R. Beasley, A. Kapitulnik, *Phys. Rev. B* **2009**, 79, 140407(R).

[22] W. Lu, P. Yang, W. D. Song, G. M. Chow, J. S. Chen *Phys. Rev. B* **2013**, 88, 214115.

[23] G. Koster, L. Klein, W. Siemons, G. Rijnders, J. S. Dodge, C. -B, Eom, D. H. A. Blank, M. R. Beasley, *Rev. Mod. Phys.* **84**, 253 (2012).

[24] R. Bachelet, F. Sánchez, J. Santiso, C. Munuera, C. Ocal, J. Fontcuberta, *Chem. Mater.* **21**, 2494 (2009).

[25] G. Koster, B. L. Kropman, G. J. H. M. Rijnders, D. H. A. Blank, H. Rogalla, *Appl. Phys. Lett.* **73**, 2920 (1998).

[26] G. Koster, G. J. H. M. Rijnders, D. H. A. Blank, H.Rogalla, *Appl. Phys. Lett.* **1999**, 74, 3729.

[27] M. Huijben, A. Brinkman, G. Koster, G. Rijnders, H. Hilgenkamp, D. H. A. Blank *Adv. Mater.* **2009**, 21, 1665.

[28] W. J. Kaiser, L. D. Bell, *Phys. Rev. Lett.* **1988**, 60, 1406.

[29] L. D. Bell, W. J. Kaiser, *Phys. Rev. Lett.* **1988**, 61, 2368.

[30] E. Haq, T. Banerjee, M. H. Siekman, J. C. Lodder, R. Jansen, *Appl. Phys. Lett.* **2005**, 86, 082502.

[31] S. Parui, K. G. Rana, L. Bignardi, P. Rudolf, B. J. van Wees, T. Banerjee, *Phys. Rev. B* **2012**, 85, 235416.

[32] M. K. Weilmeier, W. H. Rippard, R. A. Buhrman, *Phys. Rev. B* **1999**, 59, R2521.

[33] M. Sze, *Physics of Semiconductor Devices*. (Wiley, New York, 1969); E.H. Rhoderick and R.H. Williams, *Metal-Semiconductor Contacts*, 2nd Ed. (Clarendon, Oxford, 1988).

[34] H. Lu, C. Zhang, H. Guo, H. Gao, M. Liu, J. Liu, G. Collins, C. Chen, *Appl. Mat. Int.* **2010**, 2, 2496.

[35] H. Kumigashira, H. M. Minohara, M. Takizawa, A. Fujimori, D.Toyota, I. Ohkubo, M. Oshima, M. Lippmaa, M. Kawasaki, *Appl. Phys. Lett.* **2008**, 92, 122105.

[36] R. I. Eglitis, D. Vanderbilt, *Phys. Rev. B* **2008**, 77, 195408.

[37] W. Sitaputra, N. Sivadas, M. Skowronski, D. Xiao, R. M. Feenstra, *Phys. Rev. B* **2015**, 91, 205408.

[38] W. Lu, W. D. Song, K. He, J. Chai, C-J. Sun, J. Chow, J-S. Chen, *J. Appl. Phys* **2013**, 113, 063901.

[39] P. Delugas, V. Fiorentini, A. Mattoni, A. Filippetti, *Phys. Rev. B* **2015**, 91, 115315.

[40] R. T. Tung, Phys. Rev. B **2001**, 64, 205310.

[41] E. B. Guedes M. Abbate, K. Ishigami, A. Fujimori, K. Yoshimatsu, H. Kumigashira, M. Oshima, F. C. Vicentin, P. T. Fonseca, R. J. O. Mossanek, Phys. Rev. B **86**, 235127 (2012); A. J. Grutter, F. J. Wong, E. Arenholz, A. Vailionis, Y. Suzuki, Phys. Rev. B **2012**, 85, 134429 (2012).

[42] D. Pesquera, G. Herranz, A. Barla, E. Pellegrin, F. Bondino, E. Magnano, F. Sánchez, J. Fontcuberta, Nat. Commun. **2012**, 3, 1189.

[43] Y. Hikita, M. Nishikawa, T. Yajima, and H. Y. Hwang, Phys. Rev. B **2009**, 79, 073101.